The EBLM project – VIII. First results for M-dwarf mass, radius, and effective temperature measurements using *CHEOPS* light curves

M. I. Swayne [ID],[1]★ P. F. L. Maxted,[1] A. H. M. J. Triaud [ID],[2] S. G. Sousa [ID],[3] C. Broeg,[4,5] H.-G. Florén,[6]
P. Guterman,[7,8] A. E. Simon,[4] I. Boisse,[7] A. Bonfanti,[9] D. Martin,[10]† A. Santerne [ID],[7] S. Salmon,[11]
M. R. Standing,[2] V. Van Grootel,[12] T. G. Wilson [ID],[13] Y. Alibert,[4] R. Alonso,[14,15] G. Anglada Escudé,[16,17]
J. Asquier,[18] T. Bárczy,[19] D. Barrado,[20] S. C. C. Barros,[3,21] M. Battley [ID],[22,23] W. Baumjohann [ID],[9]
M. Beck,[11] T. Beck,[4] A. Bekkelien,[11] W. Benz,[4,5] N. Billot,[11] X. Bonfils,[24] A. Brandeker,[6] M.-D. Busch,[4,5]
J. Cabrera,[25] S. Charnoz,[26] A. Collier Cameron [ID],[13] Sz. Csizmadia [ID],[25] M. B. Davies,[27] M. Deleuil,[7]
A. Deline,[11] L. Delrez [ID],[12,28] O. D. S. Demangeon,[3,21] B.-O. Demory,[5] G. Dransfield,[2] D. Ehrenreich,[11]
A. Erikson,[25] A. Fortier,[4,5] L. Fossati,[9] M. Fridlund [ID],[29,30] D. Futyan,[11] D. Gandolfi [ID],[31] M. Gillon,[28]
M. Guedel,[32] G. Hébrard,[33,34] N. Heidari,[7,35,36] C. Hellier,[1] K. Heng,[5,22] M. Hobson,[37,38] S. Hoyer [ID],[7]
K. G. Isaak,[39] L. Kiss,[40,41,42] V. Kunovac Hodžić,[2] S. Lalitha,[2] J. Laskar,[43] A. Lecavelier des Etangs,[33]
M. Lendl [ID],[11] C. Lovis,[11] D. Magrin,[44] L. Marafatto,[44] J. McCormac,[22] N. Miller [ID],[1] V. Nascimbeni,[44]
G. Olofsson,[6] R. Ottensamer,[32] I. Pagano,[45] E. Pallé,[14,15] G. Peter,[46] G. Piotto,[44,47] D. Pollacco,[22]
D. Queloz,[11,48] R. Ragazzoni,[44,47] N. Rando,[18] H. Rauer,[25,49,50] I. Ribas,[16,17] N. C. Santos,[3,21]
G. Scandariato,[45] D. Ségransan,[11] A. M. S. Smith,[25] M. Steinberger,[9] M. Steller,[9] Gy. M. Szabó,[51,52]
N. Thomas,[4] S. Udry,[11] I. Walter,[46] N. A. Walton[53] and E. Willett[2]

Affiliations are listed at the end of the paper

ABSTRACT

The accuracy of theoretical mass, radius, and effective temperature values for M-dwarf stars is an active topic of debate. Differences between observed and theoretical values have raised the possibility that current theoretical stellar structure and evolution models are inaccurate towards the low-mass end of the main sequence. To explore this issue, we use the *CHEOPS* satellite to obtain high-precision light curves of eclipsing binaries with low-mass stellar companions. We use these light curves combined with the spectroscopic orbit for the solar-type companion to measure the mass, radius, and effective temperature of the M-dwarf star. Here, we present the analysis of three eclipsing binaries. We use the PYCHEOPS data analysis software to fit the observed transit and eclipse events of each system. Two of our systems were also observed by the *TESS* satellite – we similarly analyse these light curves for comparison. We find consistent results between *CHEOPS* and *TESS*, presenting three stellar radii and two stellar effective temperature values of low-mass stellar objects. These initial results from our on-going observing programme with *CHEOPS* show that we can expect to have ∼24 new mass, radius, and effective temperature measurements for very low-mass stars within the next few years.

Key words: techniques: photometric – techniques: spectroscopic – binaries: eclipsing – stars: fundamental parameters – stars: low-mass.

1 INTRODUCTION

Understanding the host star is one of the most crucial parts of exoplanet characterization. Exoplanets are mostly observed and analysed through how they affect the stellar signal, such as with the transit and radial velocity methods (Santos et al. 2020). A more accurate measurement of host size and mass thus leads to more accurate values of planetary size and mass. The host star's properties are most commonly obtained by finding the closest fit between observable star properties and stellar evolution models (e.g. Baraffe et al. 1998; Dotter et al. 2008). Therefore, any uncertainty in these models leads to systematic errors in the inferred stellar and exoplanetary properties. This has become a potential issue regarding low-mass star systems' recent popularity as targets for exoplanet observation (Charbonneau & Deming 2007; Quirrenbach et al. 2014;

★ E-mail: m.i.swayne@keele.ac.uk
† NASA Sagan Fellow.

Gillon et al. 2017; Delrez et al. 2018). Low-mass star systems suffer from a lack of data compared to more massive stars because they are intrinsically much fainter and, hence, harder to study. There is a shortfall in direct and precise mass and radius measurements of these systems, with effective temperature measurements being rarer still. The EBLM project (Triaud et al. 2013) was launched to address this lack of fundamental data for M-dwarfs. Hundreds of eclipsing binaries with low-mass companions have been identified using data from the WASP project (Pollacco et al. 2006), and we have measured the spectroscopic orbits for the primary stars in more than 100 of these EBLM systems (Triaud et al. 2017). These data are used to select targets for further study to address lack of precise mass, radius, and temperature measurements for low-mass stars, especially below 0.3 solar masses.

A number of studies have reported inconsistencies between the observed radii and M-dwarfs and theoretically predicted radii from models of low-mass stars, an effect commonly called radius inflation (e.g. Casagrande, Flynn & Bessell 2008; Torres, Andersen & Giménez 2010; Spada et al. 2013; Kesseli et al. 2018). Typically, the measured radii are larger than the predicted values for stars of a given mass by a few per cent (e.g. Morales et al. 2009). There is also a tendency for M-dwarfs to be cooler than predicted by models, such that the luminosity of the star is approximately correct. It is currently unclear to what extent radius inflation is due to problems with stellar models, or is the result of bias in the observed radius estimates. Possible sources of error from the models involve uncertainties in the input physics of the model, its initial chemical composition and in convection efficiency (Tognelli, Prada Moroni & Degl'Innocenti 2018; Fernandes et al. 2019). These would in turn provide an uncertainty to predicted radius. It is also possible that some models are missing some physical process that affects the stellar radius. The presence of a strong magnetic field or magnetic activity could inhibit the convective energy transport present in lower-mass stars (Chabrier, Gallardo & Baraffe 2007). This could result in the inflation effect, as the star attempts to maintain a constant energy flux through the surface. Rotation in eclipsing binaries has also been proposed as a potential cause. Tidal interactions between the two bodies in the system could increase the speed of the internal stellar dynamo leading to increased activity (Ribas 2006). Radius inflation therefore could be an observational bias caused by using eclipsing binaries to obtain radii from M-dwarfs. However, cases of long-period eclipsing binaries (Irwin et al. 2011) and isolated M-dwarfs (Spada et al. 2013; Van Grootel et al. 2018) showing similar inflation to short-period eclipsing binaries casts doubt on tidal interactions being the sole cause. The effect of metallicity on very low-mass stars is also debated as a possible cause for inflation with its effect on the opacity in the outer layers of the star. In their revision of the age of CM Dra, Feiden & Chaboyer (2014) find a reduction of observed mass–radius discrepancies from 6 per cent to 2 per cent upon obtaining more accurate metallicity and age measurements for this binary star. Metallicity measurements for EBLM systems are more reliable than M + M binaries like CM Dra because the spectrum of a solar-type star is much less complex and crowded than the spectrum of a rapidly rotating M-dwarf star. Radius measurements for several EBLM systems by von Boetticher et al. (2019) suggest that the metallicity may have a measurable effect on stellar radius. Therefore, the accuracy of metallicity values is important when considering the radius inflation problem. Large uncertainties in metallicity, such as those in the order of 0.2 dex as seen in Olander, Heiter & Kochukhov (2021), could lead to differences in radius residuals of ∼0.024 according to the metallicity-dependent relation described in von Boetticher et al. (2019). Finally, there has been

recent disagreement on the reality of the effect. Parsons et al. (2018) reports that 75 per cent of their objects are up to 12 per cent inflated. However, two papers in the EBLM project (Gill et al. 2019; von Boetticher et al. 2019) find little evidence of inflation in their samples of 10 and 5 objects, respectively. A much larger sample of precise and accurate mass, radius, and effective measurements for M-dwarfs of known metallicity is needed so that we can reliably estimate the properties of low-mass host stars in planetary systems.

The *CHEOPS* mission (Benz et al. 2021) is the first small (S-class) European Space Agency mission. Launched on the 18th of December 2019, it has been designed primarily to perform ultrahigh-precision photometry of bright stars that are known to host exoplanet systems. The *CHEOPS* guaranteed-time observing programme includes a small number of 'Ancillary Science' programmes, where the stars observed do not host exoplanets, but where the observations made are relevant to exoplanet science. This includes our programme to use the capabilities of *CHEOPS* to explore the radius inflation problem. Additionally, in measurements of M-dwarf effective temperature in EBLM systems, there is the possibility of some unrealized systematic error, with different studies reporting widely different results for the same object (e.g. Gómez Maqueo Chew et al. 2014; Swayne et al. 2020). Through obtaining high precision observations of secondary eclipses we can compare to previous observations and explore any potential systematic effect.

In this paper, we present our analysis of the first three targets in our *CHEOPS* observing programme with a complete set of observations – EBLM J1741+31, EBLM J1934–42, and EBLM J2046 + 06. EBLM J1741+31 and EBLM J1934–42 have also been observed by the *TESS* satellite (Ricker et al. 2015). This gives us an opportunity to test the reliability of our methods to measure mass, radius, and effective temperature by comparing the results from the two instruments. Our observations, data reduction and methods to characterize the host star are outlined in Section 2. The analysis of the light curves and results are described in Section 3. We discuss our results in the context of previous mass, radius, and effective temperature measurements for M-dwarfs in Section 4, and give our conclusions as to the future prospects for our observing programme in Section 5.

2 OBSERVATIONS AND METHODS

Our three targets are all detached eclipsing binary stars in which a solar-type star is eclipsed by an M-dwarf. The log of our observations is given in Table 1. The observations were made as part of the *CHEOPS* Guaranteed Time Observation (GTO) programme ID-037: Eclipsing binaries with very low-mass stars. This programme seeks to observe primary and secondary eclipses of 25 EBLM systems. *CHEOPS* observes stars from low-Earth orbit, so observations are interrupted by occultation of the target by the Earth and passages through the South Atlantic Anomaly. These gaps in the light curve can be up to 44 and 19 min, respectively.

The raw data were processed using version 13 of the *CHEOPS* data reduction pipeline (DRP; Hoyer et al. 2020). The DRP performs image correction for environmental and instrumental effects before performing aperture photometry of the target. As explained in Hoyer et al. (2020), the *Gaia* DR2 catalogue (Gaia Collaboration et al. 2018) is used by the DRP to simulate an observations' field of view (FoV) in order to estimate the level of contamination present in the photometric aperture. The DRP also accounts for the rotating FoV of *CHEOPS*, where other stars in the image can create 'smear' trails and contaminate the photometric aperture. The smear effect is corrected by the DRP, while the contamination produced by nearby stars is recorded in the DRP data products, allowing the user to include or

Table 1. A log of observation dates and details for each target visit. Sp. Type is the estimated spectral type of the primary star. Effic. is the fraction of the observing interval covered by valid observations of the target. R_{ap} is the aperture radius used to compute the light curve analysed in this paper.

Event	Target Sp. Type	V (mag)	Start Date (UTC)	Duration (s)	T_{exp} (s)	Effic. (per cent)	File key	R_{ap} (pixels)
Transit	J1741+31	11.7	2020-06-13T08:20:00	27794	60	67.8	CH_PR100037_TG014601_V0102	30.0
Eclipse[a]	G0V		2020-06-10T08:12:58	29098	60	63.0	CH_PR100037_TG014501_V0102	30.0
Transit	J1934−42	12.62	2020-06-27T13:43:57	28387	60	60.7	CH_PR100037_TG015001_V0100	25.0
Eclipse	G8V		2020-07-13T09:47:00	28387	60	61.1	CH_PR100037_TG014901_V0100	25.0
Transit	J2046+06	9.86	2020-08-28T22:08:00	35676	60	81.1	CH_PR100037_TG015601_V0100	25.0
Eclipse	F8V		2020-07-03T11:34:00	42313	60	66.7	CH_PR100037_TG015501_V0100	25.0

[a]Does not cover the phase of superior conjunction.

ignore the contamination correction provided. The final photometry is extracted by the DRP using three different fixed aperture sizes labelled 'RINF', 'DEFAULT' and 'RSUP' (at radii of 22.5, 25.0 and 30.0 pixels, respectively) and a further 'OPTIMAL' aperture whose size is dependent upon the FoV contamination. The observed and processed data are made available on the Data Analysis Center for Exoplanets (DACE) web platform.[1] We downloaded our data from DACE using PYCHEOPS,[2] a PYTHON module developed for the analysis of data from the *CHEOPS* mission (Maxted et al. 2021). We fitted the light curves from all four apertures and found that different choice of aperture radius has a negligible impact on the results. Therefore, for EBLM J1741+31 and EBLM J1934−42, we selected the aperture radius that gave the minimum median absolute deviation (MAD) of the point-to-point differences in the light curve of the eclipse visit. We then used the chosen aperture type for the respective transit visits. For EBLM J2046+06 this criterion resulted in slightly different aperture radii for the two visits from the preferred OPTIMAL aperture (25.5 and 26.0 pixels), so we used the DEFAULT aperture instead.

The *TESS* survey is split into overlapping $90° × 24°$ deg sky sectors over both northern and southern hemispheres with each sector being observed for approximately one month. EBLM J1741+31 (TIC 18319090) was observed in Sectors 25 and 26 of the survey as part of the Guest Investigator programmes G022156 and G022253, with 2-min cadence data made available. EBLM J1934−42 (TIC 143291764) was observed in Sectors 13 and 27 of the survey as part of the Guest Investigator programmes G011278 and G03216, with 2-min cadence data made available. Data were reduced by the Science Processing Operations Center Pipeline (SPOC; Jenkins et al. 2016) and made available from the Mikulski Archive for Space Telescopes (MAST)[3] web service. We used the Pre-search Data Conditioned Simple Aperture Photometry (PDCSAP) flux data for our analysis. Any cadences in the light curve with severe quality issues were ignored using the 'default' bitmask 175 (Tenenbaum & Jenkins 2018). The TESS light curve of EBLM J1741+31 shows a smooth variation with an amplitude ∼0.2 per cent in the flux between the transits. To remove this variability we divided the light curve by a low-order polynomial fitted by least-squares to the data between the transits. EBLM J1934−42 shows variability in the TESS light curve with an amplitude of about 1 per cent on time-scales of a few days. This may be due to moderate stellar activity modulated by stellar rotation. To remove this low-frequency noise, we fit the data between the transits with a Gaussian process (GP) calculated using the CELERITE (Foreman-Mackey et al. 2017) software package. The kernel of the GP is the stochastically driven damped simple harmonic

oscillator function defined by Foreman-Mackey et al. We then divide the entire light curve by the GP predicted by the best-fitting hyper-parameters.

The spectroscopic stellar parameters (T_{eff}, log g, microturbulence (ξ_t), [Fe/H]) and respective uncertainties were estimated by using ARES+MOOG, following the same methodology as described in Sousa (2014) and Santos et al. (2013). For this, we used the combined spectra from the individual observations done with SOPHIE for EBLM J1741+31 and with HARPS observations from ESO programme 1101.C-0721 for EBLM J1934−42 and EBLM J2046 + 06. For EBLM J1741+31, there were 13 individual observations with SOPHIE, with a signal-to-noise ratio (SNR) of 20–50. The combined spectrum has a total SNR ∼140. For EBLM J1934−42, there were 24 individual observations, with SNR varying between 15–20. The combined spectra has a total SNR ∼100. For EBLM J2046+06, there were 22 individual observations, with SNR varying between 50 and 80. The combined spectra has a total SNR ∼300. We used the ARES code[4] (Sousa et al. 2007, 2015) to measure equivalent widths (EW) of iron lines measured using the list of lines presented in Sousa et al. (2008). A minimization process assuming ionization and excitation equilibrium is used to find convergence for the best set of spectroscopic parameters. In this process, we use a grid of Kurucz model atmospheres (Kurucz 1993) and the radiative transfer code MOOG (Sneden 1973).

The radii of the three targets was determined using an adapted infrared flux method (IRFM; Blackwell & Shallis 1977) via relationships between the bolometric flux, the stellar angular diameter, the effective temperature, and the parallax, recently detailed in Schanche et al. (2020). For each target, and using a Markov chain Monte Carlo (MCMC) approach, we built spectral energy distributions (SEDs) from the ATLAS Catalogues (Castelli & Kurucz 2003), using the stellar spectral parameters derived above as priors. Subsequently, we conducted synthetic photometry by convolving the SEDs with the throughput of the selected photometric bandpasses and compared the resulting fluxes with the observed fluxes in these bandpasses; *Gaia* G, G_{BP}, and G_{RP}, 2MASS J, H, and K, and *WISE* W1 and W2 (Skrutskie et al. 2006; Wright et al. 2010; Gaia Collaboration et al. 2020) to obtain the stellar bolometric fluxes and hence the angular diameters. These diameters were combined with offset-corrected *Gaia* EDR3 parallax (Lindegren et al. 2020) to produce the stellar radii given in Table 2.

The stellar mass $M_\star$ and age $t_\star$ were inferred from two different stellar evolutionary models, namely the PARSEC[5] v1.2S code (Marigo

Table 2. The observed stellar properties of the primary star of our binary targets. Right ascension (RA) and declination (Dec.) are coordinates with equinox J2000.0.

	EBLM J1741+31	EBLM J1934−42	EBLM J2046+06
Name	TYC 2606−1838−1	TIC 143291764	TYC 524−2528−1
RA	17 41 21.27	19 34 25.69	20 46 43.88
Dec.	+31 24 55.3	−42 23 11.6	+06 18 09.7
G (mag)	11.40	11.42	9.83
$T_{\mathrm{eff},1}$ (K)	6376 ± 72	5648 ± 68	6302 ± 70
$\log g_1$ (cgs)	4.63 ± 0.11	4.33 ± 0.12	3.98 ± 0.11
ξ_t (km s^{-1})	1.25 ± 0.05	1.10 ± 0.04	1.61 ± 0.05
[Fe/H]	0.09 ± 0.05	0.29 ± 0.05	0.00 ± 0.05
R_1(R$_\odot$)	1.336 ± 0.015	0.996 ± 0.008	1.722 ± 0.015
M_1(M$_\odot$)	1.270 ± 0.043	1.046 ± 0.049	1.339 ± 0.056
Age (Gyr)	1.2 ± 0.7	1.8 ± 2.0	2.8 ± 0.6
K (km s^{-1})	37.14 ± 0.04	18.62 ± 0.01	15.55 ± 0.01

Table 3. The priors set for each target during the MultiVisit analysis.

	J1741+31	J1934−42	J2046+06
f_c	0.3003 ± 0.0016	–	− 0.1901 ± 0.0008
f_s	0.4591 ± 0.0012	–	0.5545 ± 0.0004
h_1	0.771 ± 0.012	0.729 ± 0.011	–
h_2	0.420 ± 0.050	0.398 ± 0.050	–
L	0.007 ± 0.004	–	–
$\log \rho/\rho_\odot$	− 0.274 ± 0.021	–	–

et al. 2017) and the CLES code (Code Liègeois d'Évolution Stellaire; Scuflaire et al. 2008). We adopted the stellar effective temperature T_{eff}, metallicity [Fe/H], and radius $R_{\mathrm{IRFM},\star}$ as input parameters and carried out two independent analyses. The first analysis used the Isochrone placement algorithm (Bonfanti et al. 2015; Bonfanti, Ortolani & Nascimbeni 2016), which retrieves the best estimates for both mass and age by interpolating within pre-computed PARSEC grids of isochrones and tracks. The second analysis, instead, returned the mass and age values by directly fitting the input parameters to the CLES models, following a Levenberg–Marquadt minimization (Salmon et al. 2021). Finally, we combined the two different mass and age values to obtain the definitive $M_\star$ and $t_\star$ parameters; further details can be found in Bonfanti et al. (2021). The masses obtained are given in Table 2.

The semi-amplitude of the primary star's spectroscopic orbit, K, is required for the calculations of secondary star's mass. For EBLM J1934−42 and EBLM J2046+06, we used values of K from the Binaries Escorted By Orbiting Planets survey (BEBOP; Martin et al. 2019). For J1741−31, we calculated K from a fit to radial velocity data from the SOPHIE high-resolution échelle spectrograph (Perruchot et al. 2008) mounted on the 193 cm telescope at the Observatoire de Haute-Provence (France). Twenty measurements were collected between the dates of 2019-02-24 and 2020-09-03 with a typical exposure time of 1800s, leading to a mean uncertainty of 13.7 m s^{-1}. These were obtained as part of a Large Programme aiming to detect circumbinary planets (e.g. Martin et al. 2019). The 20 spectra were obtained in High-Efficiency mode, where the resolution is reduced to 40 000 for a 2.5 × gain in throughput over the High-Resolution mode of 75 000. All observations were performed with a fibre on the science target and a fibre on the sky. The latter is used to remove background contamination originating from the Moon. All science and sky spectra were reduced using the SOPHIE Data Reduction Software (DRS) and cross-correlated with a G2 mask to obtain radial velocities. These methods are described in Baranne et al. (1996) and Courcol et al. (2015), and have been shown to produce precisions and accuracies of a few meters per seconds (e.g. Bouchy et al. 2013; Hara et al. 2020), well below what we typically obtained on this system. We used the PYTHON module ELLC (Maxted 2016) to model radial velocity. In our fit of the Keplerian orbit, we accounted for jitter by applying a weight in our log-likelihood function. We used the PYTHON module EMCEE (Foreman-Mackey et al. 2013) to sample the posterior probability distribution (PPD) of our model parameters. The stellar properties and obtained value of K are all displayed in Table 2.

3 ANALYSIS

We analyse the *CHEOPS* light curves for each star in two steps. In the first step, we analyse each *CHEOPS* visit in order to determine initial values for our model parameters, and to determine which nuisance parameters must be included in the model to deal with instrumental noise. In the second step, we analyse all the data for each star in a single MCMC analysis to obtain our final results. These results are then compared to an MCMC analysis of *TESS* data when available. The output from the light-curve analysis is then combined with as estimate of for the mass of the primary star and K to determine the mass and radius of the M-dwarf. The depth of the secondary eclipse is used together with model SEDs to estimate the effective temperature of the M-dwarf.

3.1 CHEOPS visit-by-visit analysis

To create the models needed for light-curve fitting, we used PYCHEOPS. The transit model uses the qpower2 algorithm (Maxted & Gill 2019) to calculate the transit light curve, assuming a power-2 limb darkening law. The parameters used in the model are the time of mid-primary eclipse T_0; the transit depth $D = k^2 = R_2^2/R_1^2$, where R_2 and R_1 are the radii of the secondary and primary stars; $b = a\cos i/R_1$, where i is the orbital inclination and a is the semimajor axis; $W = \sqrt{(1+k)^2 - b^2}R_1/(\pi a)$; the eccentricity and argument of periastron-dependent parameters $f_s = \sqrt{e}\sin(\omega)$ and $f_c = \sqrt{e}\cos(\omega)$; the eclipse depth L and the limb-darkening parameters h_1 and h_2 as defined by Maxted (2018). For an eclipsing binary with a circular orbit, D, W, and b are the depth, width (in phase units), and impact parameter of the eclipse, respectively. For each target, we obtained one primary and one secondary eclipse so the orbital period, P, has to be fixed at a known value. For EBLM J1741+31 and EBLM J1934−42, we fixed P to the value obtained from our analysis of the *TESS* light curve. For EBLM J2046+06, we fixed the orbital period at the value reported by Martin et al. (2019). To better constrain our fit, Gaussian priors were put on f_c and f_s, using e and ω measurements from the spectroscopic orbit. The orbital eccentricity of EBLM J1934−42 is very small, so we assumed a circular orbit for our analysis. For EBLM J1741+31 and EBLM J1934−42, which have partial eclipses, the eclipses do not constrain the limb darkening properties of the star so we place Gaussian priors on h_1 and h_2. These priors are listed in Table 3. The values of h_1 and h_2 appropriate for the values of [Fe/H], $T_{\mathrm{eff},1}$, and $\log g$ given in Section 2 are found using interpolation in the data tables presented in Maxted (2018) based on the limb-darkening profiles from the STAGGER-grid (Magic et al. 2015). An offset (0.01 for h_1, −0.045 for h_2) was then applied based on the offset between empirical and tabulated values of these limb darkening parameters observed in the *Kepler* bandpass by Maxted (2018).

CHEOPS light curves can be affected by trends correlated with satellite roll angle, the varying contamination of the photometric aperture, the background level in the images, and the estimated

correction for smear trails from nearby stars. These trends are modelled using linear decorrelation against these parameters, or for roll angle ϕ, $\sin(\phi)$, $\cos(\phi)$, $\sin(2phi)$, etc. The coefficients for each trend are optimized simultaneously with the parameters of the transit or eclipse model in a least-squares fit to all the data in each visit. In the case of the eclipse events, fits to individual visits were performed with all orbital parameters apart from eclipse depth fixed at the parameters derived from the fit to the transit. To select decorrelation parameters for each visit, we did an initial fit to each light curve with no decorrelation and used the rms of the residuals from this fit, σ_p, to set a normal prior on the decorrelation parameters, $\mathcal{N}(0, \sigma_p)$ or, for df/dt, $\mathcal{N}(0, \sigma_p/\Delta t)$ where Δt is the duration of the visit. We then added decorrelation parameters to the fit one by one, selecting the parameter with the lowest Bayes factor $B_p = \mathrm{e}^{-(p/\sigma_p)^2/2} \sigma_0/\sigma_p$ at each step, where σ_0 is the standard error on the decorrelation parameter from the least-squares fit (Maxted et al. 2021). We stop adding decorrelation parameters when $B_p > 1$ for all remaining parameters. This process sometimes leads to a set of parameters including some that are strongly correlated with one another and so are therefore not well determined; i.e., they have large Bayes factors. We therefore go through a process of repeatedly removing the parameter with the largest Bayes factor if any of the parameters have a Bayes factors $B_p > 1$. The second step of this process typically removes no more than one or two parameters.

3.2 CHEOPS MultiVisit analysis

We used the MULTIVISIT function in PYCHEOPS to do a combined analysis of both visits for each target. Decorrelation against trends with roll angle were done implicitly using the method described in Maxted et al. (2021), i.e. by modifying the calculation of the likelihood to account for the decorrelation against roll angle without explicitly calculating the nuisance parameters df/dsin(ϕ), df/dcos(ϕ), etc. The same Gaussian priors for f_c and f_s, h_1 and h_2 were used as for the analysis of individual visits. For EBLM J1741+31, we also set a priors on the eclipse depth L and on the log of the stellar density $log\rho$, which is directly related to the transit parameters via Kepler's law (Maxted et al. 2021). This target has no detectable secondary eclipse and the primary eclipse is very shallow so the model parameters are poorly constrained by the light curve alone. The prior on eclipse depth was set using the predicted flux ratio. This ratio was calculated using the predicted absolute G-band magnitude, M_G, for each star based on their masses using the calibration by Pecaut & Mamajek (2013). The scatter around the M_G–mass relation for M-dwarfs was assumed to be similar to the observed scatter in M_V magnitude values reported by Hartman et al. (2015). The prior for $log\rho$ was calculated, using the derived values of mass and radius described in Section 2. The values used for these priors are shown in Table 3.

The joint PPD for the model and nuisance parameters are sampled, using the sampler EMCEE (Foreman-Mackey et al. 2013). The initial parameters of the run were the values previously obtained by the fits to the individual visit. We sampled a chain of 128 walkers each going through 35 000 steps after a 'burn-in' of 1024 steps to ensure that the sampler has converged to a steady state. To ensure adequate sampling, we ensured that the number of steps chosen was more than 50 times longer than the autocorrelation length of each fitted parameter chain. For EBLM J1934–42, this required a second run of EMCEE with 180 000 steps, and for EBLM J1741+31, a second run with 240 000 steps with a 'burn-in' of 8192 steps. To ensure independent random samples from their posterior probability distributions, each parameter chain was thinned by approximately half the minimum parameter autocorrelation length. The parameter values given in

Table 4 are the median value of the parameters from the sampled PPD and the standard errors are estimated from the 15.9 per cent and 89.1 per cent percentile-points in the distribution for each parameter. The fitted decorrelation parameters from our analyses are shown in Appendix A in Table A1. Correlations between selected parameters are displayed in Appendix B. In EBLM J1741+31, there are very strong correlations between D, W and b as can be seen in Fig. B1. In EBLM J1934–42, the correlation between these parameters is not as strong though there are a significant number of walkers that tend to larger values of D and b as can be seen in Fig. B2. In EBLM J2046+06 as shown in Fig. B3, there is again a correlation between D, W and b, but not as strongly as for EBLM J1741+31. The light-curve fit and residuals for these parameter values are shown in Fig. 1.

3.3 TESS light curve analysis

We have compared our results using CHEOPS data to a similar analysis of the TESS light curves for EBLM J1741+31 and EBLM J1934–42. For EBLM J1741+31, we used data from TESS sectors 25 and 26 covering five transits. For EBLM J1934–42, we used data from sectors 13 and 27 covering 6 transits. Sampling of the PPD of our model parameters was again performed using EMCEE. Gaussian priors were set on f_c and f_s using the same spectroscopically derived values as in the *CHEOPS* fit. Gaussian priors were also set on h_1 and h_2, using the stellar parameters given in Section 2 and assuming the same offset, but using the *TESS* passband to interpolate our values. For EBLM J1741+31 a prior on eclipse depth L was again set using the predicted flux ratio of the target, adjusting to M_{Ic} magnitudes from Pecaut & Mamajek (2013) due to the different passband of *TESS*. EBLM J1741+31 required more steps than EBLM J1934–42 to ensure the number of steps in the simulation was more than 50 times longer than the autocorrelation length in each parameter chain. We sampled a chain of 128 walkers each going through 20 480 steps for EBLM J1934–42 and 81 920 steps for EBLM J1741+31, with initial orbital parameters determined by a least-squares fit of the light curves. To allow the walkers to settle into the probability distributions, we performed a burn-in of 2560 and 5120 steps before the sampling for EBLM J1934–42 and EBLM J1741+31, respectively. The parameter values given in Table 4 are the median value of the parameters from the sampled PPD and the standard errors are estimated from the 15.9 per cent and 89.1 per cent percentile-points in the distribution for each parameter. In EBLM J1741+31, similarly to the *CHEOPS* light curve, there are very strong correlations between D, W, and b as can be seen in Fig. B4. In EBLM J1934–42, the correlation between these parameters is not as strong. Though there are a small amount of walkers that tend to larger values of D and b as can be seen in Fig. B5, this is a smaller trend than in the *CHEOPS* light curve. The light-curve fit and residuals are shown in Fig. 2.

3.4 Mass, radius, and effective temperature

To obtain values of companion mass and radius, we made use of the function MASSRADIUS in PYCHEOPS. The M-dwarf mass is determined from the assumed primary mass M_1, orbital period P, orbital eccentricity e, the sine of orbital inclination $\sin(i)$, and the semi-amplitude of the star's spectroscopic orbit K. The M-dwarf radius is determines from the primary star radius R_1 from Table 2 and the planet–star radius ratio from the light-curve analysis, k. The value of $log\,g_2$ in Table 4 is determined directly from K and the parameters of the transit light curve using equations (4) from Southworth, Wheatley & Sams (2007).

Table 4. The derived orbital parameters for each *CHEOPS* target calculated by our `pycheops` fit. The eclipse depths displayed are in the relevant instrumental bandpass.

	J1741+31		J1934–42		J2046+06
	CHEOPS	*TESS*	*CHEOPS*	*TESS*	*CHEOPS*
Model parameters					
T_0 (BJD)	2014.0490 ± 0.0001	1990.9112 ± 0.0001	2028.2295 ± 0.0002	1659.7836 ± 0.0002	2090.6246 ± 0.0001
P (days)	$=7.71263$	7.71263 ± 0.00004	$=6.35251$	6.35251 ± 0.00001	$=10.10779$
D	0.152 ± 0.024	0.109 ± 0.011	0.0513 ± 0.0047	0.0485 ± 0.0011	0.0161 ± 0.0002
W	0.0091 ± 0.0016	0.0118 ± 0.0008	0.0190 ± 0.0002	0.0189 ± 0.0001	0.0263 ± 0.0002
b	1.312 ± 0.061	1.184 ± 0.041	0.797 ± 0.027	0.785 ± 0.009	0.165 ± 0.096
f_c	0.3006 ± 0.0016[a]	0.3003 ± 0.0015[a]	$=0.0$	$=0.0$	-0.1902 ± 0.0006[a]
f_s	0.4595 ± 0.0012[a]	0.4590 ± 0.0012[a]	$=0.0$	$=0.0$	0.5545 ± 0.0004[a]
L	$-$	$-$	0.00126 ± 0.00032	0.00250 ± 0.00019	0.00039 ± 0.00005
h_1	0.768 ± 0.012[a]	0.818 ± 0.011[a]	0.729 ± 0.011[a]	0.784 ± 0.011[a]	0.757 ± 0.011
h_2	0.435 ± 0.050[a]	0.397 ± 0.050[a]	0.398 ± 0.050[a]	0.394 ± 0.050[a]	0.393 ± 0.178
Derived parameters					
R_2/R_1	0.390 ± 0.031	0.330 ± 0.017	0.2266 ± 0.0102	0.2202 ± 0.0025	0.1268 ± 0.0007
R_1/a	0.0621 ± 0.0003	0.0610 ± 0.0004	0.0639 ± 0.0014	0.0634 ± 0.0007	0.0743 ± 0.0005
R_2/a	0.0224 ± 0.0019	0.0191 ± 0.0011	0.0139 ± 0.0010	0.0137 ± 0.0003	0.0094 ± 0.0001
i (°)	85.32 ± 0.22	85.86 ± 0.17	87.08 ± 0.16	87.15 ± 0.06	89.30 ± 0.41
e	0.3015 ± 0.0015	0.3009 ± 0.0015	0.0	0.0	0.3437 ± 0.0005
ω (°)	56.81 ± 0.16	56.81 ± 0.16	$-$	$-$	108.93 ± 0.06
Absolute parameters					
M_2 ($M_\odot$)	0.4786 ± 0.0095	0.4783 ± 0.0095	0.1864 ± 0.0055	0.1864 ± 0.0055	0.1975 ± 0.0053
R_2 ($R_\odot$)	0.521 ± 0.042	0.441 ± 0.023	0.226 ± 0.010	0.2193 ± 0.0031	0.2184 ± 0.0023
$\log g_2$ (cgs)	4.758 ± 0.069	4.917 ± 0.046	5.008 ± 0.043	5.039 ± 0.014	5.073 ± 0.008
$T_{\mathrm{eff},2}$ (K)	$-$	$-$	3023 ± 96	3030 ± 41	3199 ± 57

[a]Derived parameters based on Gaussian priors shown in Table 3.

The ratio of the eclipse depths is directly related to the surface brightness ratio, i.e. $F_2/F_1 = L/D$, where F_2 is the flux per unit area integrated of the observing bandpass for star 2, and similarly for F_1. The surface brightness is directly related to a star's effective temperature, so we can use this information together with the values of $T_{\mathrm{eff},1}$, $\log g_1$, and [Fe/H] from Table 2, and SEDs from model stellar atmospheres to determine $T_{\mathrm{eff},2}$, the effective temperature of the M-dwarf. We calculated integrated surface brightness values for a large range of effective temperature, surface gravity, and metallicity, using PHOENIX model atmospheres with no alpha-element enhancement (Husser et al. 2013) for both the *CHEOPS* or *TESS* bandpasses. We then sample the PPD for $T_{\mathrm{eff},2}$, using EMCEE and interpolation within this grid using the value of $\log g_2$ from Table 4. The results are given in Table 4.

3.5 J1741+31 eclipse visit

Unfortunately, there is no secondary eclipse visible in the *CHEOPS* light curve for EBLM J1741+31. We found that the predicted time of superior conjunction for our fitted model parameters is outside the duration of our scheduled *CHEOPS* visit. This visit was scheduled based on a preparatory analysis, using less data than is now available for this target. We can use the analysis of the transit in the *CHEOPS* light curve to calculate the minimum separation of the stars around superior conjunction. We find that the probability that there is a secondary eclipse is <0.002 per cent. This explains why there is also no secondary eclipse visible in the *TESS* light curve (Fig. 2).

4 DISCUSSION

Observations of EBLM systems with *CHEOPS* are complementary to the data provided by the *TESS* mission. The *CHEOPS* instrument response extends much further to the blue than *TESS*. Looking for

consistency of the transit parameters measured by the two instruments makes it possible to check for colour-dependent systematic errors, e.g. contamination of the photometry by other stars in the line of sight. Our results for EBLM J1741+31 and EBLM J1934–42 show good agreement between the results from the analysis of the *CHEOPS* and *TESS* light curves. *CHEOPS* is also able to observe regions of the sky not covered by the *TESS* survey, e.g. close to the ecliptic. The precision of the parameters derived per transit from each instrument are similar so the final radius measurement from the *TESS* data will be more precise in cases where it has observed many transits. *CHEOPS* observations can be scheduled to cover individual transit or eclipse events, which can be advantageous if we want to observe long-period systems.

Our results for EBLM J2046+06 show that *CHEOPS* light curves can be used to measure radii accurate to about 1 per cent and T_{eff} accurate to about 2 per cent for the M-dwarf in EBLM systems with well-defined transits. This is sufficient for our main goal of establishing an empirical mass-radius-metallicity relation for very low mass stars. Observations of 24 additional EBLM binaries with well-defined transits with *CHEOPS* are on-going. The results presented here have already been used by Maxted et al. (2021) to constrain the properties of the host star in their study of the super-Earth GJ 1132 b using *CHEOPS* observations of the transit.

The transit model in PYCHEOPS does not account for surface features on the primary star due to magnetic activity, e.g. dark spots, faculae, or plages. The impact of these features on the parameters derived is dependent on whether they are occulted by the secondary star or not (Czesla et al. 2009; Pont et al. 2013; Oshagh et al. 2013). Dark spots occulted during the transit will produce small peaks in the light curve. If these are not accounted for in the model then the transit depth will be underestimated, leading to an underestimate for the companion radius. The opposite is true for dark spots not occulted by the companion. We checked the TESS and WASP
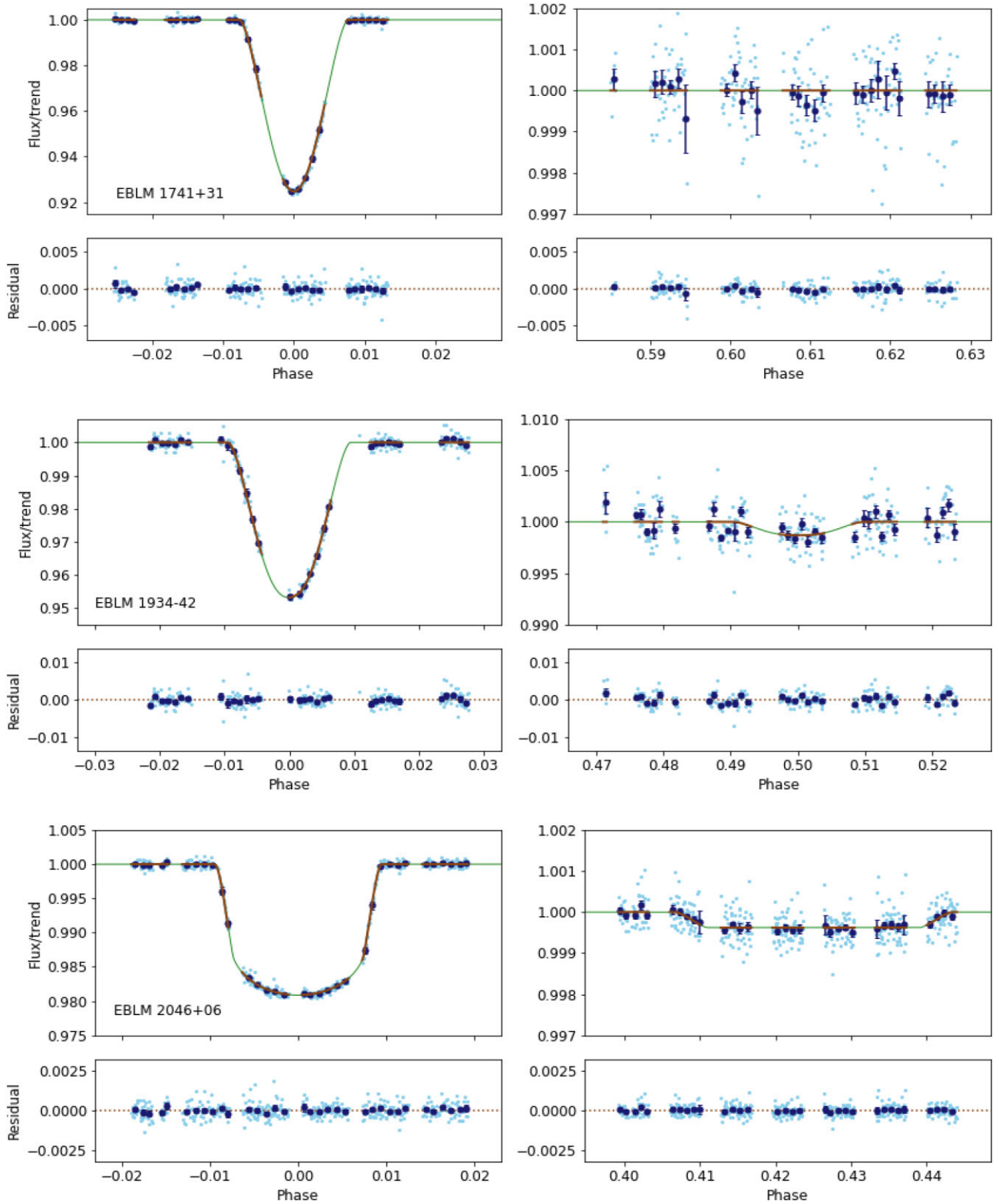
Figure 1. Fitted light curve of EBLM J1741+31 (*Top*), EBLM J1934–42 (*Middle*), and EBLM J2046+06 (*Bottom*) in phase intervals around the transit and eclipse events. The observed data corrected for instrumental trends according to the decorrelation coefficients given in Table A1 are shown in cyan. The transit and eclipse models are shown in green. Binned data points with error bars are shown in blue and the fit between binned data points in brown. The residual of the fit is displayed below the fitted curves.
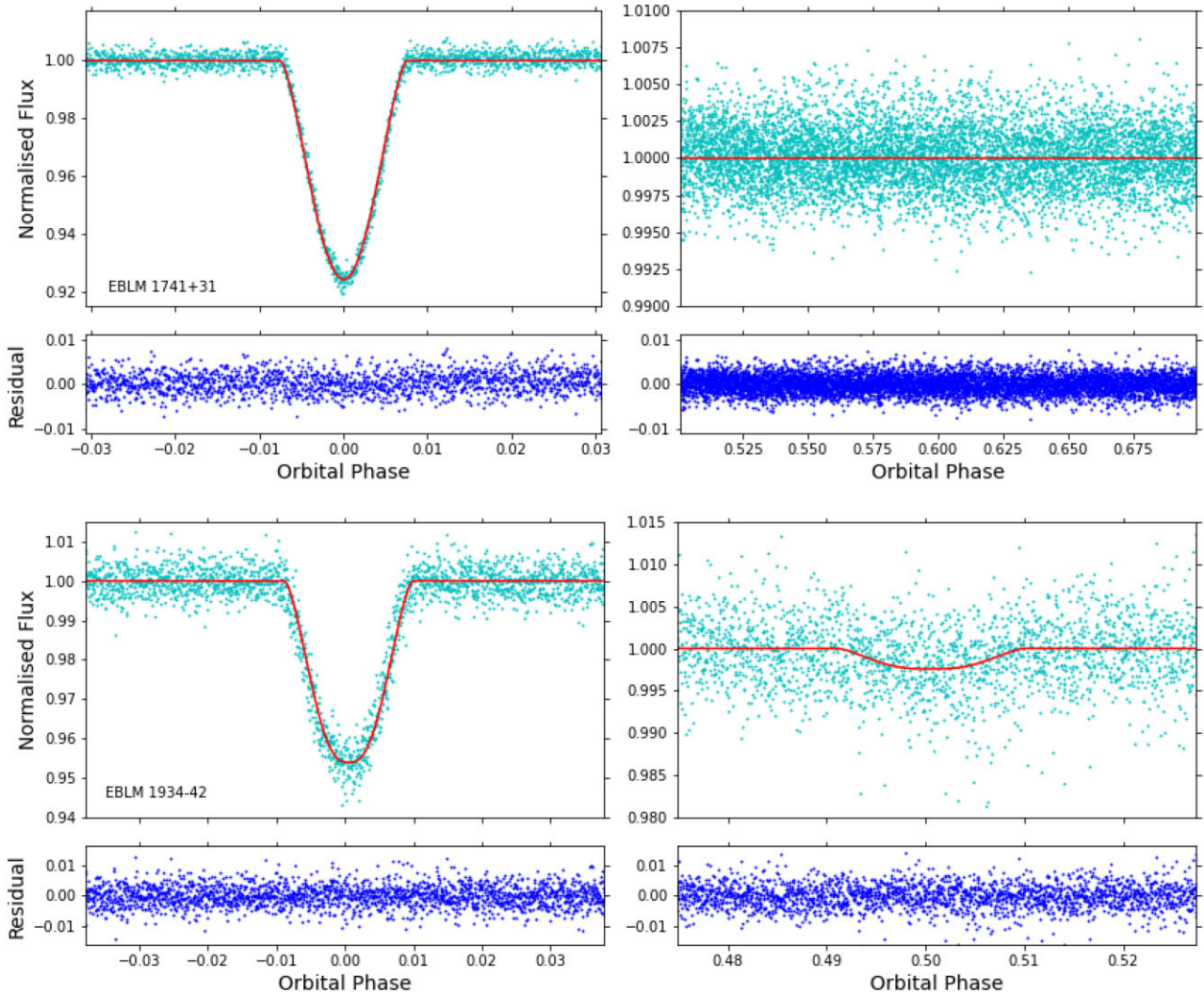
Figure 2. Fitted *TESS* light curve of EBLM J1741+31 (top) and EBLM J1934–42 (bottom) in phase intervals around the transit and eclipse events. The observed data points are shown in cyan. The fitted light curve is shown in red. The residual of the fit is displayed below the fitted curves in blue.

light curves of our targets for variability on time scales of a few days or more due to the combination of rotation and magnetic activity. For all three targets we find that any such variability has an amplitude $\lesssim 1$ per cent ($\lesssim 0.1$ per cent for EBLM J2046+06). Spots near the poles of these slowly rotating solar-type stars are not expected, so we conclude that magnetic activity has a negligible impact on the parameters we have derived for the M-dwarfs in these systems.

Our results are shown in the context of other mass, radius, and effective temperature measurements for M-dwarfs in Fig. 3. EBLM J1741+31 and EBLM J1934–42 follow the trend for stars with masses $\lesssim 0.5\,M_\odot$ to be larger on average by a few per cent than predicted by models that do not account for magnetic activity. The radius of EBLM J2046+06, which is our most precise radius measurement, agrees well with the models of Baraffe et al. (2015). EBLM J1934–42 is a metal-rich star, which may be consistent with the idea that metallicity has an influence on radius inflation (e.g. Berger et al. 2006; Spada et al. 2013; von Boetticher et al. 2019). Not shown in Fig. 3 are the masses and radii for M-dwarfs in EBLM binaries by von Boetticher et al. (2019) and Gill et al. (2019). We do not yet have effective temperature measurements for these M-dwarfs, but the methods we have developed here can be applied to

the *CHEOPS* and *TESS* light curves for those stars, as well as other EBLM binaries observed by these instruments, to provide a more complete picture for these systems.

5 CONCLUSIONS

In this paper, we have reported the first results of our *CHEOPS* observing programme on low-mass eclipsing binaries. We find that the very high precision of the photometry from this instrument and the possibility to schedule observations of individual transit and eclipse events are well-matched to our science goal of measuring an empirical mass–radius–metallicity relation for very low-mass stars. We report three M-dwarf radii and two effective temperatures between our three targets contributing to the rather sparse amount of data at the low-mass end of the H–R diagram. Additional observations from our on-going observations with *CHEOPS* complemented by further analysis of data from the *TESS* mission will provide precise and accurate mass, radius, and $T_{\rm eff}$ measurements for many very low-mass stars of known metallicity and age. Fundamental data of this quality will be essential if we are to find an answer to the long-standing radius inflation problem.
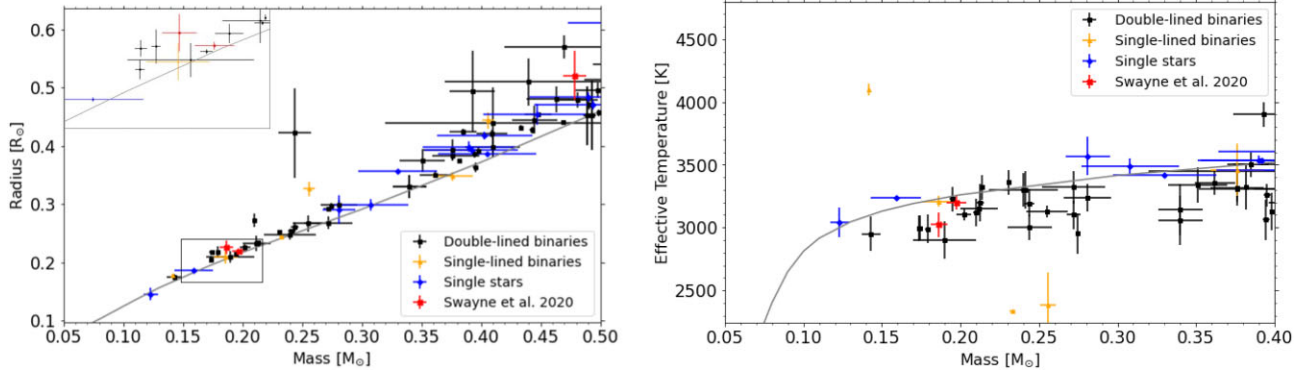
Figure 3. *Left*: A cut-out of the stellar mass versus stellar radius diagram, using results from Nefs et al. (2013), Gillen et al. (2017), and Parsons et al. (2018) with our results highlighted in red. The type of system is displayed by different colours. The theoretical relation from Baraffe et al. (2015) for an age of 1 Gyr is plotted in grey. *Right*: A cut-out of the stellar mass versus effective temperature diagram, using results from Nefs et al. (2013), Gillen et al. (2017), and Parsons et al. (2018) with our results highlighted in red. The type of system is displayed by different colours. The theoretical relation from Baraffe et al. (2015) for an age of 1 Gyr is plotted in grey.

DATA AVAILABILITY

The CHEOPS data underlying this article are available in its online supplementary material. The fitted light curve is available at CDS via anonymous ftp to cdsarc.u-strasbg.fr (130.79.128.5) or via https://cdsarc.unistra.fr/viz-bin/cat/J/MNRAS.

This paper includes data collected by the TESS mission, which is publicly available from the Mikulski Archive for Space Telescopes (MAST) at the Space Telescope Science Institure (STScI) (https://mast.stsci.edu). Funding for the TESS mission is provided by the NASA Explorer Program directorate. STScI is operated by the Association of Universities for Research in Astronomy, Inc., under NASA contract NAS 5-26555. We acknowledge the use of public TESS Alert data from pipelines at the TESS Science Office and at the TESS Science Processing Operations Center.

REFERENCES

Baraffe I., Chabrier G., Allard F., Hauschildt P. H., 1998, A&A, 337, 403
Baraffe I., Homeier D., Allard F., Chabrier G., 2015, A&A, 577, A42
Baranne A. et al., 1996, A&AS, 119, 373
Benz W. et al., 2021, Exp. Astron., 51, 109
Berger D. H. et al., 2006, ApJ, 644, 475
Blackwell D. E., Shallis M. J., 1977, MNRAS, 180, 177
Bonfanti A., Ortolani S., Piotto G., Nascimbeni V., 2015, A&A, 575, A18
Bonfanti A., Ortolani S., Nascimbeni V., 2016, A&A, 585, A5
Bonfanti A. et al., 2021, A&A, 646, A157
Bouchy F., Díaz R. F., Hébrard G., Arnold L., Boisse I., Delfosse X., Perruchot S., Santerne A., 2013, A&A, 549, A49
Casagrande L., Flynn C., Bessell M., 2008, MNRAS, 389, 585
Castelli F., Kurucz R. L., 2003, in Piskunov N., Weiss W. W., Gray D. F., eds, IAU Symp. Vol. 210, Modelling of Stellar Atmospheres. p. A20, preprint (astro-ph/0405087)
Chabrier G., Gallardo J., Baraffe I., 2007, A&A, 472, L17
Charbonneau D., Deming D., 2007, preprint (arXiv:0706.1047)
Courcol B. et al., 2015, A&A, 581, A38
Czesla S., Huber K. F., Wolter U., Schröter S., Schmitt J. H. M. M., 2009, A&A, 505, 1277
Delrez L. et al., 2018, in Marshall H. K., Spyromilio J., eds, SPIE Conf. Ser. Vol. 10700, Ground-based and Airborne Telescopes VII. SPIE, Bellingham, p.107001I
Dotter A., Chaboyer B., Jevremović D., Kostov V., Baron E., Ferguson J. W., 2008, ApJS, 178, 89

Feiden G. A., Chaboyer B., 2014, A&A, 571, A70
Fernandes C. S., Van Grootel V., Salmon S. J. A. J., Aringer B., Burgasser A. J., Scuflaire R., Brassard P., Fontaine G., 2019, ApJ, 879, 94
Foreman-Mackey D., Hogg D. W., Lang D., Goodman J., 2013, PASP, 125, 306
Foreman-Mackey D., Agol E., Ambikasaran S., Angus R., 2017, AJ, 154, 220
Gaia Collaboration et al., 2018, A&A, 616, A1
Gaia Collaboration et al., 2021, A&A, 649, A1
Gill S. et al., 2019, A&A, 626, A119
Gillen E., Hillenbrand L. A., David T. J., Aigrain S., Rebull L., Stauffer J., Cody A. M., Queloz D., 2017, ApJ, 849, 11
Gillon M. et al., 2017, Nature, 542, 456
Gómez Maqueo Chew Y. et al., 2014, A&A, 572, A50
Hara N. C. et al., 2020, A&A, 636, L6
Hartman J. D. et al., 2015, AJ, 149, 166
Hoyer S., Guterman P., Demangeon O., Sousa S. G., Deleuil M., Meunier J. C., Benz W., 2020, A&A, 635, A24
Husser T. O., Wende-von Berg S., Dreizler S., Homeier D., Reiners A., Barman T., Hauschildt P. H., 2013, A&A, 553, A6
Irwin J. M. et al., 2011, ApJ, 742, 123
Jenkins J. M. et al., 2016, in Chiozzi G., Guzman J. C., eds, SPIE Conf. Ser. Vol. 9913, Software and Cyberinfrastructure for Astronomy IV. SPIE, Bellingham, p. 99133E
Kesseli A. Y., Muirhead P. S., Mann A. W., Mace G., 2018, AJ, 155, 225
Kurucz R. L., 1993, SYNTHE Spectrum Synthesis Programs and Line Data. Smithsonian Astrophysical Observatory, Cambridge, MA
Lindegren L., et al., 2021, A&A, 649, A4
Magic Z., Chiavassa A., Collet R., Asplund M., 2015, A&A, 573, A90
Marigo P. et al., 2017, ApJ, 835, 77
Martin D. V. et al., 2019, A&A, 624, A68
Maxted P. F. L., 2016, A&A, 591, A111
Maxted P. F. L., 2018, A&A, 616, A39
Maxted P. F. L., Gill S., 2019, A&A, 622, A33
Maxted P. F. L., et al., 2021, MNRAS, submitted
Morales J. C. et al., 2009, ApJ, 691, 1400
Nefs S. V. et al., 2013, MNRAS, 431, 3240
Olander T., Heiter U., Kochukhov O., 2021, A&A, 649, A103
Oshagh M., Santos N. C., Boisse I., Boué G., Montalto M., Dumusque X., Haghighipour N., 2013, A&A, 556, A19
Parsons S. G. et al., 2018, MNRAS, 481, 1083
Pecaut M. J., Mamajek E. E., 2013, ApJS, 208, 9
Perruchot S. et al., 2008, in McLean I. S., Casali M. M., eds, SPIE Conf. Ser. Vol. 7014, Ground-based and Airborne Instrumentation for Astronomy II. SPIE, Bellingham, p. 70140J
Pollacco D. L. et al., 2006, PASP, 118, 1407
Pont F., Sing D. K., Gibson N. P., Aigrain S., Henry G., Husnoo N., 2013, MNRAS, 432, 2917
Quirrenbach A. et al., 2014, in Ramsay S. K., McLean I. S., Takami H., eds, SPIE Conf. Ser. Vol. 9147, Ground-based and Airborne Instrumentation for Astronomy V. SPIE, Bellingham, p. 91471F
Ribas I., 2006, Ap&SS, 304, 89
Ricker G. R. et al., 2015, J. Astron. Telesc. Instr. Syst., 1, 014003
Salmon S. J. A. J., Van Grootel V., Buldgen G., Dupret M. A., Eggenberger P., 2021, A&A, 646, A7
Santos N. C. et al., 2013, A&A, 556, A150
Santos N. C., Barros S. C. C., Demangeon O. D. S., Faria J. P., 2020, Detection and Characterization Methods of Exoplanets. Oxford Univ. Press, Oxford, p. 189
Schanche N. et al., 2020, MNRAS, 499, 428
Scuflaire R., Théado S., Montalbán J., Miglio A., Bourge P.-O., Godart M., Thoul A., Noels A., 2008, Ap&SS, 316, 83
Skrutskie M. F. et al., 2006, AJ, 131, 1163
Sneden C. A., 1973, PhD thesis, Univ. Texas at Austin
Sousa S. G., 2014, ARES+MOOG: A Practical Overview of an Equivalent Width (EW) Method to Derive Stellar Parameters. Springer International Publishing, Cham, p. 297

Sousa S. G., Santos N. C., Israelian G., Mayor M., Monteiro M. J. P. F. G., 2007, A&A, 469, 783

Sousa S. G. et al., 2008, A&A, 487, 373

Sousa S. G., Santos N. C., Adibekyan V., Delgado-Mena E., Israelian G., 2015, A&A, 577, A67

Southworth J., Wheatley P. J., Sams G., 2007, MNRAS, 379, L11

Spada F., Demarque P., Kim Y. C., Sills A., 2013, ApJ, 776, 87

Swayne M. I., Maxted P. F. L., Hodžić V. K., Triaud A. H. M. J., 2020, MNRAS, 498, L15

Tenenbaum P., Jenkins J., 2018, Technical Report, Tess Science Data Products Description Document. EXP-TESS-ARC-ICD-0014 Rev D

Tognelli E., Prada Moroni P. G., Degl'Innocenti S., 2018, MNRAS, 476, 27

Torres G., Andersen J., Giménez A., 2010, A&AR, 18, 67

Triaud A. H. M. J. et al., 2013, A&A, 549, A18

Triaud A. H. M. J. et al., 2017, A&A, 608, A129

Van Grootel V. et al., 2018, ApJ, 853, 30

von Boetticher A. et al., 2019, A&A, 625, A150

Wright E. L. et al., 2010, AJ, 140, 1868

APPENDIX A: DECORRELATION PARAMETERS

See Table A1.

Table A1. The decorrelation parameters fitted from the *CHEOPS* MultiVisit MCMC analysis. The effects these parameters represent are as follows: image background level (dfdbg), PSF centroid position (dfdx, dfdy) time (dfdt), aperture contamination (dfdcontam), and smear correction (dfdsmear).

Target	Visit	dfdbg (10^{-3})	dfdx 10^{-4}	dfdy 10^{-3}	dfdt $(10^{-2}\,\mathrm{d}^{-1})$	dfdcontam 10^{-3}	dfdsmear 10^{-4}
EBLM J1741+31	Transit	–	–	–	–	–	–
	Eclipse	–	–	–	–	–	–
EBLM J1934–42	Transit	-0.023 ± 1.491	–	-1.66 ± 0.37	–	–	–
	Eclipse	–	–	-0.38 ± 0.33	-1.04 ± 0.13	-3.25 ± 0.79	–
EBLM 2046+06	Transit	–	–	–	–	-0.55 ± 0.15	–
	Eclipse	–	-2.25 ± 0.56	0.40 ± 0.05	–	–	9.45 ± 1.72

APPENDIX B: CORRELATION DIAGRAMS FOR SELECTED PARAMETERS

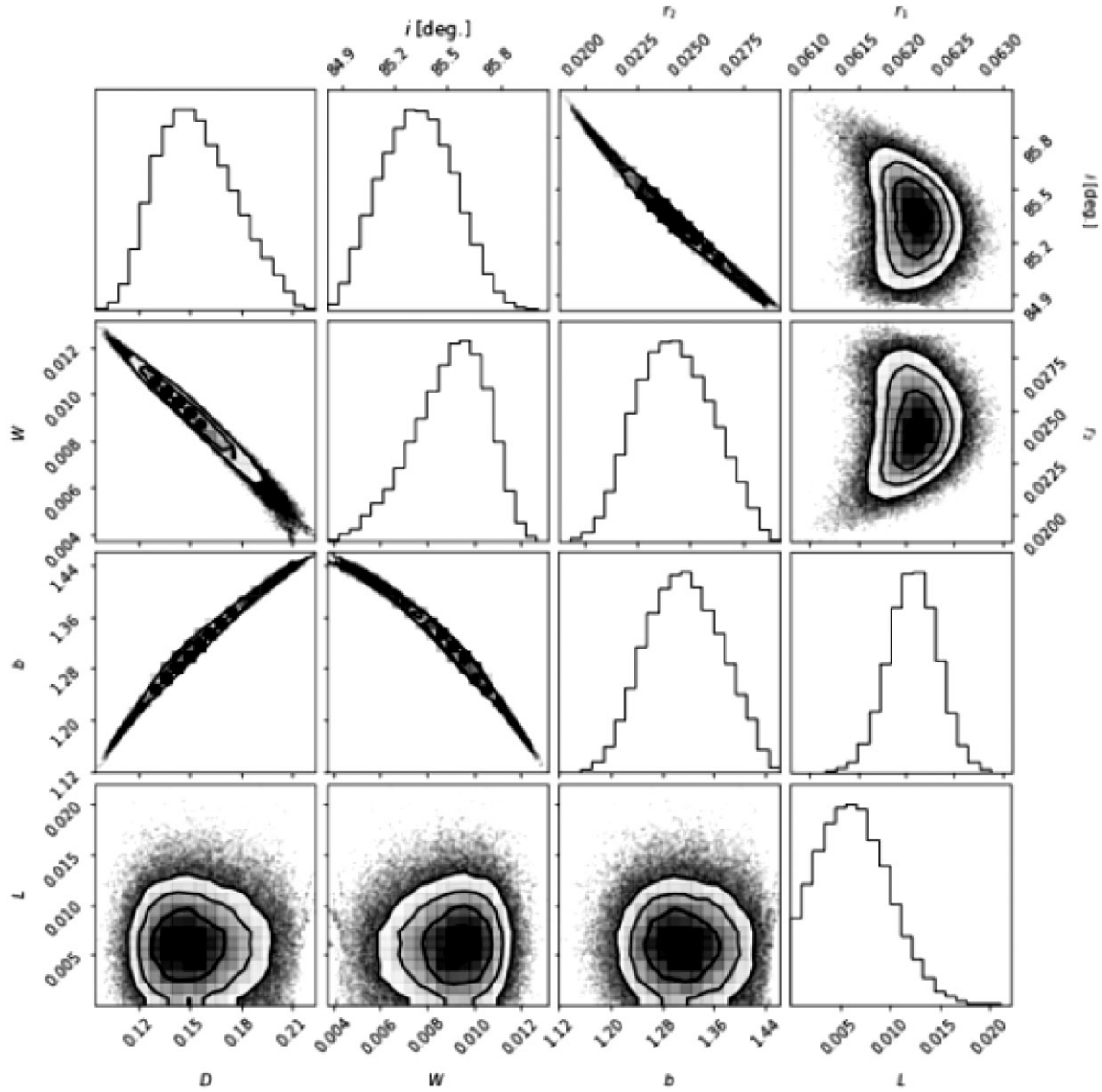See Figs B1−B5.

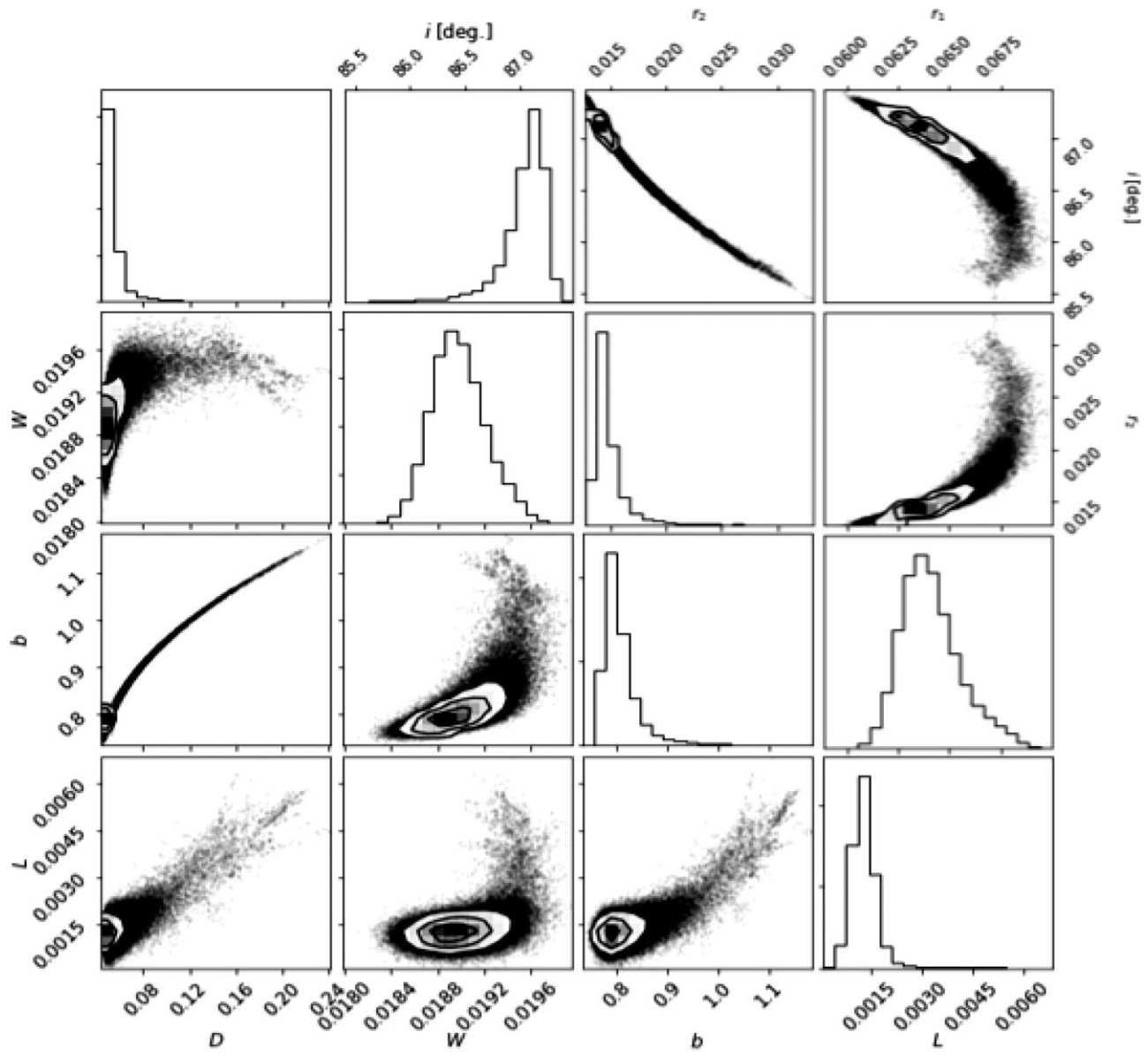**Figure B1.** Corner plot for *CHEOPS* data set of EBLM J1741+31.

Figure B2. Corner plot for *CHEOPS* data set of EBLM J1934–42.
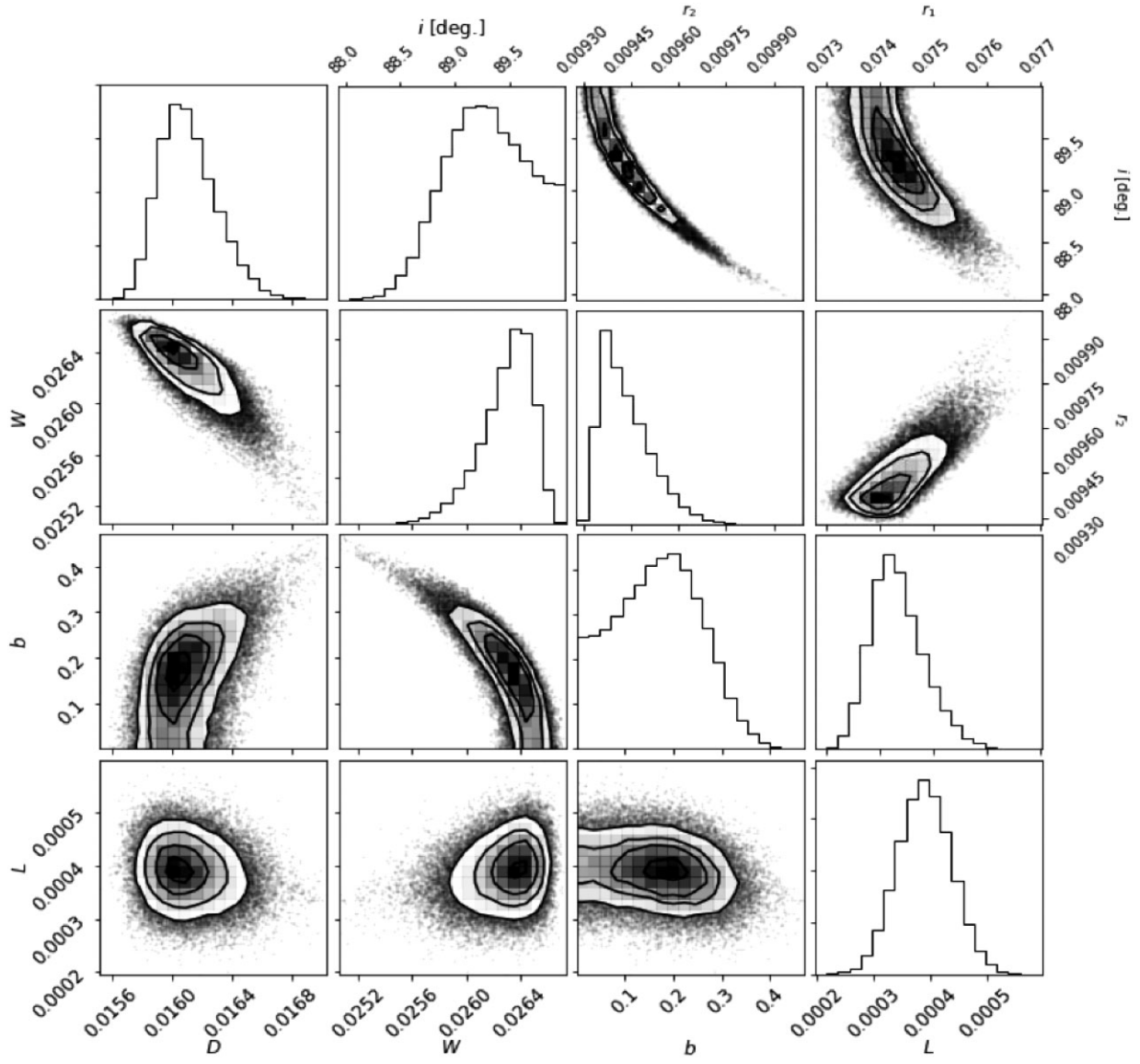
Figure B3. Corner plot for *CHEOPS* data set of EBLM J2046+06.
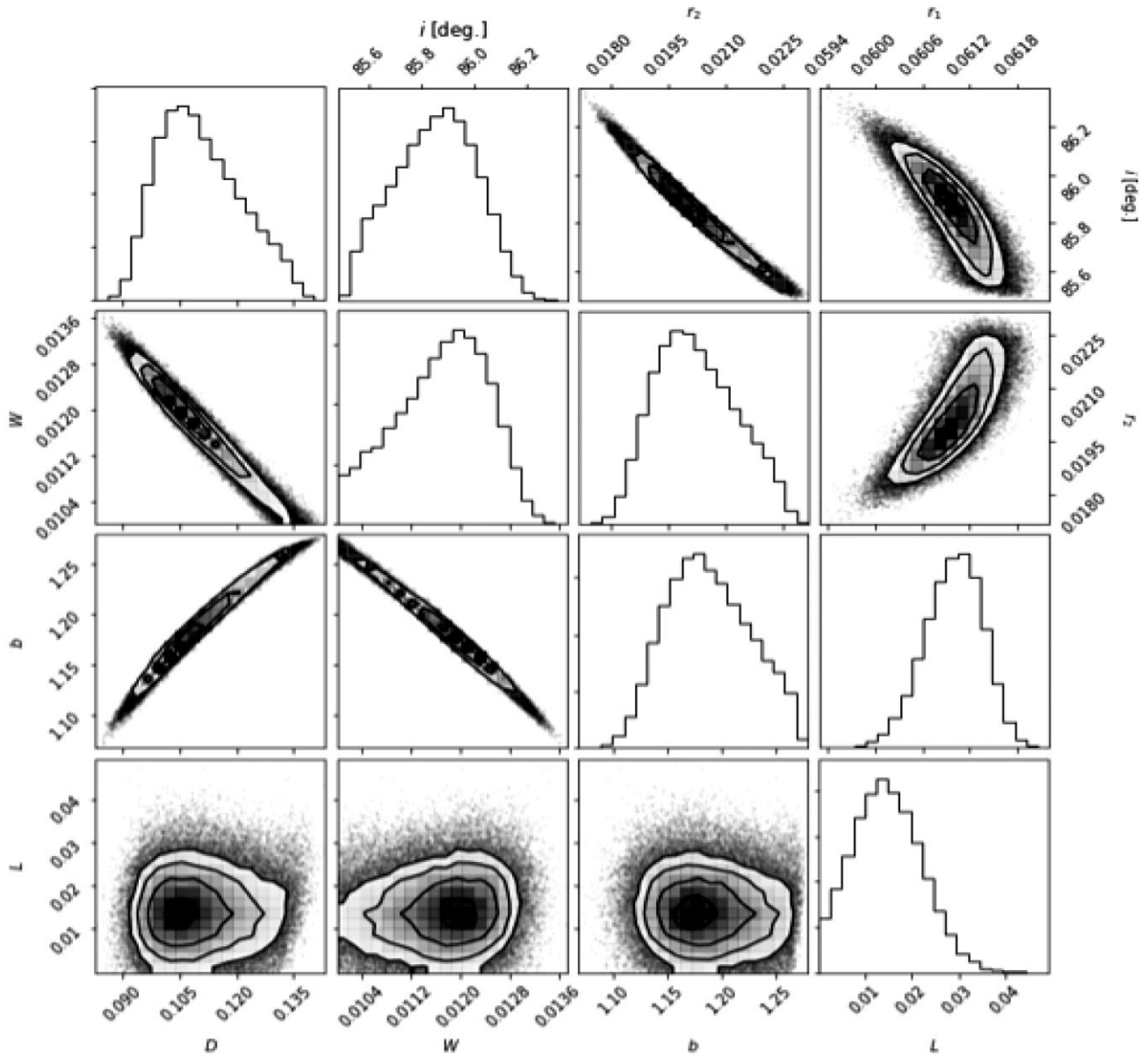
Figure B4. Corner plot for *TESS* data set of EBLM J1741+31.
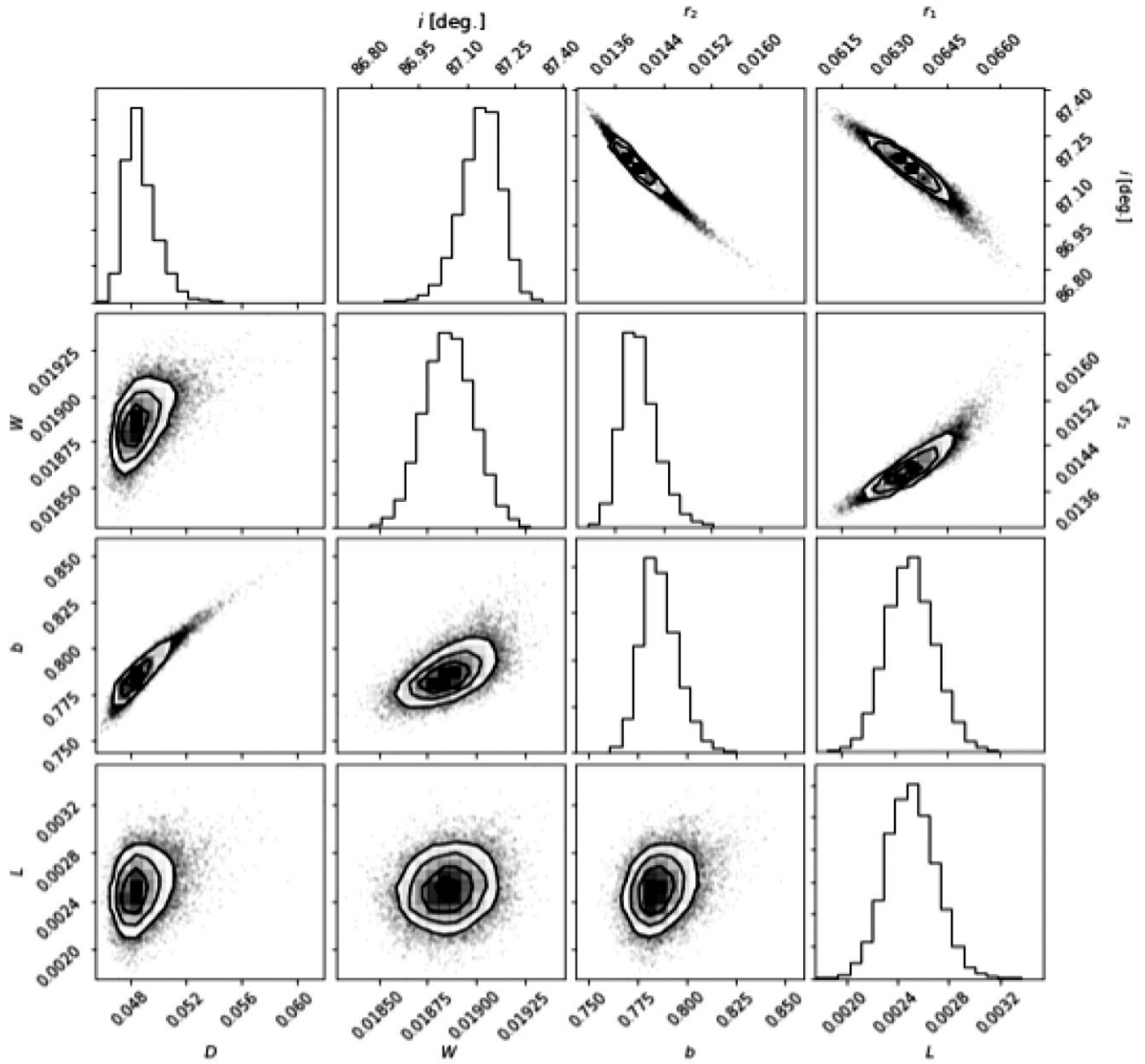
Figure B5. Corner plot for *TESS* data set of EBLM J1934–42.

[1]*Astrophysics Group, Keele University, Staffordshire ST5 5BG, UK*

[2]*School of Physics and Astronomy, University of Birmingham, Edgbaston, Birmingham B15 2TT, UK*

[3]*Instituto de Astrofísica e Ciências do Espaço, Universidade do Porto, CAUP, Rua das Estrelas, P-4150-762 Porto, Portugal*

[4]*Physikalisches Institut, University of Bern, Gesellsschaftstrasse 6, CH-3012 Bern, Switzerland*

[5]*Center for Space and Habitability, Gesellsschaftstrasse 6, CH-3012 Bern, Switzerland*

[6]*Department of Astronomy, Stockholm University, AlbaNova University Center, SE-10691 Stockholm, Sweden*

[7]*Aix Marseille Univ, CNRS, CNES, LAM, 38 rue Frédéric Joliot-Curie, 13388 Marseille, France*

[8]*Division Technique INSU, BP 330, F-83507 La Seyne cedex, France*

[9]*Space Research Institute, Austrian Academy of Sciences, Schmiedlstrasse 6, A-8042 Graz, Austria*

[10]*Department of Astronomy, The Ohio State University, Columbus, OH 43210, USA*

[11]*Observatoire Astronomique de l'Université de Genève, Chemin Pegasi 51, 1290 Versoix, Switzerland*

[12]*Space sciences, Technologies and Astrophysics Research (STAR) Institute, Université de Liège, Allée du 6 Août 19C, B-4000 Liège, Belgium*

[13]*Centre for Exoplanet Science, SUPA School of Physics and Astronomy, University of St Andrews, North Haugh, St Andrews KY16 9SS, UK*

[14]*Instituto de Astrofísica de Canarias, E-38200 La Laguna, Tenerife, Spain*

[15]*Departamento de Astrofísica, Universidad de La Laguna, E-38206 La Laguna, Tenerife, Spain*

[16]*Institut de Ciències de l'Espai (ICE, CSIC), Campus UAB, Can Magrans s/n, E-08193 Bellaterra, Spain*

[17]*Institut d'Estudis Espacials de Catalunya (IEEC), E-08034 Barcelona, Spain*

[18]*ESTEC, European Space Agency, NL-2201AZ Noordwijk, the Netherlands*

[19]*Admatis, 5. Kandó Kálmán Street, 3534 Miskok, Hungary*

[20]*Depto. de Astrofísica, Centro de Astrobiologia (CSIC-INTA), ESAC campus, E-28692 Villanueva de la Cãda (Madrid), Spain*

[21]*Departamento de Física e Astronomia, Faculdade de Ciências, Universidade do Porto, Rua do Campo Alegre, P-4169-007 Porto, Portugal*

[22]*Department of Physics, University of Warwick, Gibbet Hill Road, Coventry CV4 7AL, UK*

[23]*Centre for Exoplanets and Habitability, University of Warwick, Gibbet Hill Road, Coventry CV4 7AL, UK*

[24]*Université Grenoble Alpes, CNRS, IPAG, F-38000 Grenoble, France*

[25]*Institute of Planetary Research, German Aerospace Center (DLR), Rutherfordstrasse 2, D-12489 Berlin, Germany*

[26]*Université de Paris, Institut de physique du globe de Paris, CNRS, F-75005 Paris, France*

[27]*Lund Observatory, Dept. of Astronomy and Theoretical Physics, Lund University, Box 43, SE-22100 Lund, Sweden*

[28]*Astrobiology Research Unit, Université de Liège, Allée du 6 Août 19C, B-4000 Liège, Belgium*

[29]*Leiden Observatory, University of Leiden, PO Box 9513, NL-2300 RA Leiden, the Netherlands*

[30]*Department of Space, Earth and Environment, Chalmers University of Technology, Onsala Space Observatory, SE-43992 Onsala, Sweden*

[31]*Dipartimento di Fisica, Università degli Studi di Torino, via Pietro Giuria 1, I-10125, Torino, Italy*

[32]*Department of Astrophysics, University of Vienna, Tuerkenschanzstrasse 17, A-1180 Vienna, Austria*

[33]*Institut d'astrophysique de Paris, UMR7095 CNRS, Université Pierre & Marie Curie, 98bis blvd. Arago, F-75014 Paris, France*

[34]*Observatoire de Haute-Provence, CNRS, Université d'Aix-Marseille, F-04870 Saint-Michel l'Observatoire, France*

[35]*Department of Physics, Shahid Beheshti University, Tehran 1983969411, Iran*

[36]*Laboratoire J.-L. Lagrange, Observatoire de la Côte d'Azur (OCA), Universite de Nice-Sophia Antipolis (UNS), CNRS, Campus Valrose, F-06108 Nice Cedex 2, France*

[37]*Millennium Institute for Astrophysics, Casilla 36-D, Santiago, Chile*

[38]*Instituto de Astrofísica, Facultad de Física, Pontificia Universidad Católica de Chile, Av. Vicuña Mackenna 4860, 782-0436 Macul, Santiago, Chile*

[39]*Science and Operations Department - Science Division (SCI-SC), Directorate of Science, European Space Agency (ESA), European Space Research and Technology Centre (ESTEC), Keplerlaan 1, NL-2201-AZ Noordwijk, the Netherlands*

[40]*Konkoly Observatory, Research Centre for Astronomy and Earth Sciences, 1121 Budapest, Konkoly Thege Miklós út 15-17, Hungary*

[41]*ELTE Eötvös Loránd University, Institute of Physics, Pázmány Péter sétány 1/A, 1117 Budapest, Hungary*

[42]*Sydney Institute for Astronomy, School of Physics A29, University of Sydney, NSW 2006, Australia*

[43]*IMCCE, UMR8028 CNRS, Observatoire de Paris, PSL Univ., Sorbonne Univ., 77 av. Denfert-Rochereau, F-75014 Paris, France*

[44]*INAF, Osservatorio Astronomico di Padova, Vicolo dell'Osservatorio 5, I-35122 Padova, Italy*

[45]*INAF, Osservatorio Astrofisico di Catania, Via S. Sofia 78, I-95123 Catania, Italy*

[46]*Institute of Optical Sensor Systems, German Aerospace Center (DLR), Rutherfordstrasse 2, D-12489 Berlin, Germany*

[47]*Dipartimento di Fisica e Astronomia 'Galileo Galilei', Università degli Studi di Padova, Vicolo dell'Osservatorio 3, I-35122 Padova, Italy*

[48]*Cavendish Laboratory, JJ Thomson Avenue, Cambridge CB3 0HE, UK*

[49]*Center for Astronomy and Astrophysics, Technical University Berlin, Hardenberstrasse 36, D-10623 Berlin, Germany*

[50]*Institut für Geologische Wissenschaften, Freie Universität Berlin, D-12249 Berlin, Germany*

[51]*ELTE Eötvös Loránd University, Gothard Astrophysical Observatory, 9700 Szombathely, Szent Imre h. u. 112, Hungary*

[52]*MTA-ELTE Exoplanet Research Group, 9700 Szombathely, Szent Imre h. u. 112, Hungary*

[53]*Institute of Astronomy, University of Cambridge, Madingley Road, Cambridge CB3 0HA, UK*

This paper has been typeset from a TEX/LATEX file prepared by the author.